LANGMUIR

pubs.acs.org/Langmuir Article

Chemically Driven Multimodal Locomotion of Active, Flexible Sheets

Raj Kumar Manna, Oleg E. Shklyaev, and Anna C. Balazs*

Cite This: *Langmuir* 2023, 39, 780−789 Read Online

ACCESS | Metrics & More | Article Recommendations | Supporting Information

ABSTRACT: The inhibitor−promoter feedback loop is a vital component in regulatory pathways that controls functionality in living systems. In this loop, the production of chemical *A* at one site promotes the production of chemical *B* at another site, but *B* inhibits the production of *A*. In solution, differences in the volumes of the reactants and products of this reaction can generate buoyancy-driven fluid flows, which will deform neighboring soft material. To probe the intrinsic interrelationship among chemistry, hydrodynamics, and fluid−structure interactions, we model a bio-inspired system where a flexible sheet immersed in solution encompasses two spatially separated catalytic patches, which drive the *A*−*B* inhibitor−promotor reaction. The convective rolls of fluid generated above the patches can circulate inward or outward depending on the chemical environment. Within the regime displaying chemical oscillations, the dynamic fluid−structure interactions morph the shape of the sheet to periodically "fly", "crawl", or "swim" along the bottom of the confining chamber, revealing an intimate coupling between form and function in this system. The oscillations in the sheet's motion in turn affect the chemical oscillations in the solution. In the regime with non-oscillatory chemistry, the induced flow still morphs the shape of the sheet, but now, the fluid simply translates the sheet along the length of the chamber. The findings reveal the potential for enzymatic reactions in the body to generate hydrodynamic behavior that modifies the shape of neighboring soft tissue, which in turn modifies both the fluid dynamics and the enzymatic reaction. The findings indicate that this non-linear dynamic behavior can be playing a critical role in the functioning of regulatory pathways in living systems.

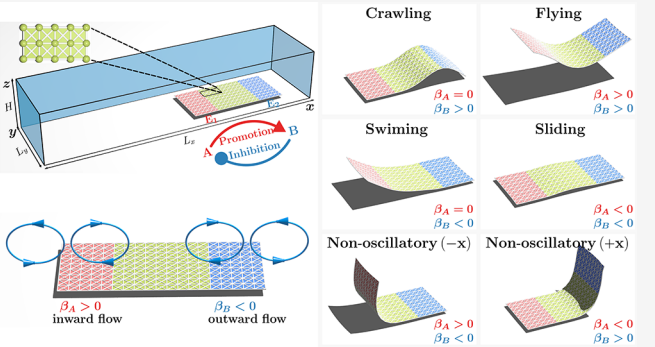

INTRODUCTION

Chemically active matter commonly refers to synthetic materials with built-in mechanisms for converting chemical energy into mechanical motion, mimicking chemo-mechanical transduction in living systems.[1−4] For example, catalyst-coated, active particles display chemo-mechanical transduction as reactants in solution trigger a catalytic reaction and the energy released from catalysis is converted into mechanical energy, which propels both the motion of the particles and the flow of surrounding fluid.[5−7] For active, non-deformable particles, the convective fluid flow cannot, however, morph the particles' shape. Conversely, computational modeling on active, flexible sheets indicates that the generated fluid flow not only transports the sheets but also deforms the shape of these soft layers.[3] For the latter systems, the interactions among chemical, hydrodynamic, and mechanical properties yield rich dynamic behavior, which remains largely unexplored. In initial studies,[3] the interactions between flowing fluids and immersed sheets were regulated by simple, one-step chemical reactions. Inspired by the functionality of feedback loops in biological systems,[8,9] here, we model the behavior of a flexible sheet that encompasses two terminal catalytic patches, which enable a promoter−inhibitor reaction in the solution. While relatively simple, the latter feedback loop can yield non-linear behavior, including periodic oscillations in chemical concentrations.[10−14] To uncover potential sources of non-linear dynamics, we determine how chemical regulation by this two-step reaction affects the temporal and spatial behavior of the responsive, mechanically compliant sheet. As we show below, the inhibitor−promotor reaction instigates fluid flow at both ends of the rectangular sheet. Depending on the properties of the reagents, the two flows can circulate in the same or opposite directions and thus trigger multimodal locomotion from the "crawling" to the "flying" of the sheet. In effect, the fluid morphs the shape of the sheet to perform a particular function, indicating a route for connecting form and function in soft active materials.

In the human body, functionality is regulated by a chain of interlinked chemical reactions.[15−18] These chemical reaction networks (CRNs) operate in fluids that are confined between soft structural walls, such as those bounding cells and internal

Received: September 28, 2022
Revised: December 16, 2022
Published: January 5, 2023

https://doi.org/10.1021/acs.langmuir.2c02666
Langmuir 2023, 39, 780−789

organs.[19] Based on findings on synthetic materials systems,[3] it is conceivable that these reaction networks trigger flow in the confined biological fluids. Furthermore, the ensuing fluid−structure interactions between the flow and the adjacent soft structural walls could be affecting the chemical kinetics in the CRNs.[20] This cross-talk among the CRNs, the host fluid, and the bounding walls is typically ignored in models for CRNs in living systems. The latter models also commonly neglect the spatial layout of the CRNs in the body;[21] the arrangement and spatial separation of the reaction sites does, however, affect the outcome of these reactions.[22−25] Hence, we may be lacking a complete picture of the system's dynamics due to the inherent coupling among chemo-mechanical transductions, the confined fluids, and the fluid−structure interactions in the body.

While the CRNs regulating living systems are highly complex, many of the pathways can be broken down into smaller, modular feedback loops.[11] Researchers have synthetized and combined equivalent modular loops to construct CRNs displaying the desired biomimetic behavior, e.g., producing oscillations and auto-amplifications of chemicals in solution.[22−26] Herein, we focus on one of the simplest modular loops: the promotor−inhibitor interaction. Figure 1 provides a schematic of the system: immersed, microscopic sheets are decorated with two spatially separated patches of surface-bound catalysts. In the presence of the appropriate reactants, the catalytic reaction at patch 1 promotes the reaction at patch 2, and the reaction at patch 2 suppresses reaction at patch 1.

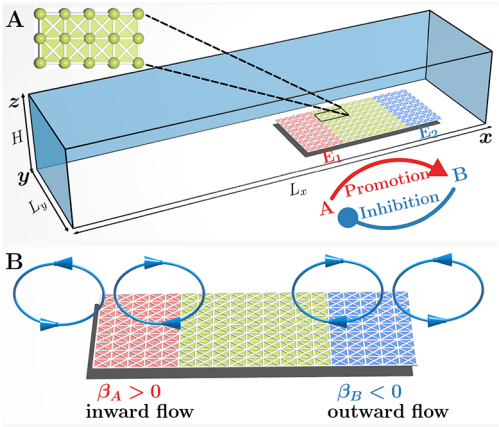

Figure 1. Schematic of an enzyme-coated elastic sheet in a fluid-filled chamber that supports the promotion and inhibition of chemical reactions. (A) The elastic sheet is coated with two enzymes, E_1 (red) and E_2 (blue), that are separated by a passive region (green) of distance R. The enzyme E_1 promotes the production of chemical B, and the enzyme E_2 inhibits the production of chemical A. The inset shows the network of nodes (marked by green dots) that form the sheet and the flexible bonds between nodes (white lines). (B) The chemical transformations of the reactants A and B at the two enzymatic patches generate fluid flow in the chamber. The direction of fluid flow (marked in blue arrows) depends on sign of the solutal expansion coefficients of chemicals A and B, β_A and β_B.

The conversion of reactants to products at the catalytic patches gives rise to fluid flow. We assume that this chemically generated flow is due to solutal buoyancy, which occurs when the reactants and generated products occupy different volumes.[27−29] These differences in volume lead to local gradients in the fluid density that in turn generate a mechanical force, which acts on the fluid and thereby produces flow in the microchamber. The magnitude of this force is dependent on the values of the solutal expansion coefficient, β_i, which characterizes the density of a fluid when a specific concentration of chemical i is present in the solution relative to the density of the pure fluid (e.g., water). The values of β_i indicate the directionality of the fluid flow (i.e., away or toward the catalytic patches) and thus control the overall flow in the chamber.

The β_i values are known for a broad range of chemicals that participate in enzymatic and catalytic reactions. In previous studies, we used the known experimental values in our model to make direct comparison with the corresponding experiments.[20,30] To date, however, there have been no comparable experiments on the systems described here and thus, we consider a broad range of β_i to identify possible behavior that could emerge in the physical systems. The design choices in creating these systems are relatively large; for a sheet of fixed shape, the designer can choose from different (1) networks of catalytic reactions and (2) spatial layouts of the associated CRNs. By performing simulations for a span of β_i, we can begin to comprehend how the designer's choices affect the functioning of the sample. As shown below, for a specific range of β_i values, the sheets display not only chemically dependent, controllable locomotion, but also self-oscillations in the fluid. In all the following examples, the system seamlessly converts chemical energy into mechanical motion and thus can accelerate the development of self-operating machines with self-sustained functionality.

Notably, analogous multimodal locomotion of flexible sheets has been achieved using magneto-elastic materials in the presence of an external magnetic field.[31] Sitti and co-workers designed magneto-elastic sheets that adaptively navigate different fluid-filled confined environments with different modes of locomotion.[32] Moreover, these magneto-elastic millirobots can exhibit locomotion over a hybrid liquid−solid environment, which demonstrates their potential for use in in vivo medical applications. Multimodal locomotion was also achieved in the aquatic environment with light-responsive liquid crystal gels that show crawling, walking, jumping, and swimming behaviors in the response to spatiotemporal light illumination.[33] Furthermore, the light stimuli were used in NIR-active liquid crystal elastomer sheets to generate other modes of multimodal locomotion, such as sliding, rotating, and rolling.[34]

The system described below exemplifies a more biomimetic design approach. Motion is instigated by the introduction of chemical "nutrients", and the active sheets enable chemo-mechanical transduction that turns fuel into sustained movement. This materials system can facilitate the development of standalone soft robots that do not involve external fields, stimuli, or extraneous electronics to drive their mechanical actions. Hence, design rules can be formulated in terms of choosing the appropriate chemical reactions and reactants to achieve the desired range of movements. Consequently, these machines can be more portable than other systems, simply needing a small vial of chemicals to autonomously perform self-sustained work.

MATERIALS AND METHODS

We consider a fluid-filled chamber that contains chemicals A and B, and a mobile elastic sheet (Figure 1A). The sheet is coated with enzymes E_1 (marked in red) and E_2 (marked in blue) that are separated by a distance R. The widths of both the enzymatic patches

https://doi.org/10.1021/acs.langmuir.2c02666
Langmuir 2023, 39, 780−789

are the same and taken as w. In the presence of substrate S, the enzyme E_1 produces chemical A and the enzyme E_2 transforms chemical A into chemical B;

$$S \xrightarrow{E_1} A \tag{1}$$

$$S + A \xrightarrow{E_2} B \tag{2}$$

The above two catalytic reactions resemble the two-step pathway of the biosynthesis of glutathione that occurs in living organisms. In contrast to the living cells where the two enzymes are homogeneously mixed and the reaction leads to a steady state, two enzymes in our system are separated by a distance. The spatial separation between these two catalytic reactions introduces the time delay required for transporting the participating reactants across the enzymatic patches. This time delay between the production and transformation of the reactants enables chemical oscillations in the system. In addition to the above catalytic reactions, the concentration of chemicals A and B decreases over time and the chemical transformations to some final products are not modeled explicitly. We also assume that concentrations of the initial reactants (substrate S) and the final products are time-independent and the reverse reactions are neglected.

We consider that the catalytic chemical reactions on the surface of the sheet are coupled to the motion of the surrounding fluid through a solutal buoyancy mechanism. Namely, the enzymes decompose the chemical reactants into products, which can occupy different volumes than the reactants and thus alter the local density of the fluid. The products can occupy different volumes than the reactants, leading to local density variations in the fluid, which gives rise to a buoyancy force per unit volume, $\boldsymbol{F}^{\mathrm{b}}$, that acts on the fluid. The force is expressed as $\boldsymbol{F}^{\mathrm{b}} = \boldsymbol{g}\rho_0 \sum \beta_i C_i$, where ρ_0 is the solvent density, $\boldsymbol{g}$ is gravitational acceleration, C_i is the concentration of chemical species i, and $\beta_i = \frac{1}{\rho_0}\frac{\partial \rho}{\partial C_i}$ are the corresponding solutal expansion coefficients. This buoyancy force density, $\boldsymbol{F}^{b}$, drives the spontaneous motion of the fluid. In other words, the immobile catalytic patch works as a "chemical pump" that drives the fluid flow via the solutal buoyancy[27] mechanism. Along the bottom surface, if the density of the products is less than the density of the reactants, the flow will move toward the patch, and this flow is referred to as "inward" flow (see schematic in Figure 1). Alternatively, if the products are denser than the reactants, the fluid flow on the bottom surface is away from the patch and is referred to as "outward" flow. In the system considered here, the temperature changes due to chemical reaction are neglected.[28,29] We also neglect any enthalpic changes associated with the mixture of the chemicals.

The viscous stresses generated by the fluid flow change the position and shape of the immersed elastic sheet, which is modeled as an initially planar network of nodes, with positions $\boldsymbol{r}_k$, that are interconnected by elastic rods (inset of Figure 1A). The nodes of the sheet experience body forces, $\boldsymbol{F}^{\mathrm{sheet}} = \boldsymbol{F}^{\mathrm{e}} + \boldsymbol{F}^{\mathrm{s}} + \boldsymbol{F}^{\mathrm{g}}$, which are the respective elastic, steric, and gravity forces. The elastic forces, $\boldsymbol{F}^{\mathrm{e}}$, are characterized by the stretching (κ_{s}) and bending (κ_{b}) moduli and are governed by the linear constitutive relations for a Kirchoff rod[35] (see the SI). The steric forces on the sheet, $\boldsymbol{F}^{\mathrm{s}}$, are the sum of the "node−node" (nn) repulsion between two nodes, $\boldsymbol{F}^{\mathrm{nn}}$, and repulsion between nodes and any of the six confining walls, $\boldsymbol{F}^{\mathrm{nw}}$. These steric forces are calculated as the gradient of a Morse potential that ensures the equilibrium separation between node−node or node−wall to be r_0 (see the SI). Gravity acting on the sheet is described by $\boldsymbol{F}^{\mathrm{g}} = V(\rho_{\mathrm{s}} - \rho_0)\boldsymbol{g}$, where V is the effective volume of each node and the density of the sheet (ρ_{s}) is assumed to be greater than the density of the solvent (ρ_0). In the absence of reactants, the sheet sediments settle to the bottom of the chamber.

The dynamic interactions between the elastic sheet and flowing fluid are described by the respective continuity and Navier−Stokes (in the Boussinesq approximation[36]) equations for the dynamics of an incompressible flow and the equation for the velocity of the nodes of the elastic sheet:

$$\nabla \cdot \boldsymbol{u} = 0 \tag{3}$$

$$\frac{\partial \boldsymbol{u}}{\partial t} + (\boldsymbol{u}\cdot\nabla)\boldsymbol{u} = -\frac{1}{\rho_0}\nabla p + \nu\nabla^2\boldsymbol{u} + \frac{1}{\rho_0}\boldsymbol{F} \tag{4}$$

where

$$\boldsymbol{F} = \underbrace{\boldsymbol{g}\,\rho_0 \sum \beta_i C_i}_{\text{solutal buoyancy}} + \underbrace{\frac{1}{V}\left(\boldsymbol{F}^{\mathrm{e}} + \sum \boldsymbol{F}^{\mathrm{nn}} + \sum \boldsymbol{F}^{\mathrm{nw}}\right) + (\rho_{\mathrm{s}} - \rho_0)\boldsymbol{g}}_{\text{sheet}}$$

$$\frac{\partial \boldsymbol{r}_{\mathrm{k}}}{\partial t} = \boldsymbol{u} \tag{5}$$

Here, the body force per unit volume, $\boldsymbol{F}$, acting on the fluid arises due to the solutal buoyancy force density and the body force density exerted by the sheet on the fluid. The immersed boundary method (IBM)[35] is used to treat the fluid−structure interactions. In the IBM, the velocity of each node of the sheet is determined by the fluid velocity at the position of the node (eq 3). Also, $\boldsymbol{u}$ and p are the local fluid velocity and pressure, respectively, ν is the kinematic viscosity of the fluid, and ∇ is the spatial gradient operator.

The dynamics of dissolved chemical species C_i in the chamber is governed by an advection−diffusion−reaction equation:

$$\frac{\partial C_i}{\partial t} + (\boldsymbol{u}\cdot\nabla)C_i = D_i\nabla^2 C_i - \gamma_i C_i + \underbrace{K_d^{E_1}\sum \delta(\boldsymbol{r}_{E_1} - \boldsymbol{r})}_{E_1} + \underbrace{K_d^{E_2}\sum \delta(\boldsymbol{r}_{E_2} - \boldsymbol{r})}_{E_2} \tag{6}$$

Here, D_i is the diffusion constant for the ith reagent of concentration C_i. γ_i is the deactivation rate constant of chemical i. The chemical reactions occur at the position of the catalytic node $\boldsymbol{r}_k$. The consumption and production of chemicals at the enzymatic patches are described by

$$K_d^{E_1} = \begin{cases} k_{E_1}F_1(C_B) \text{ for } A \\ 0 \text{ for } B \end{cases}, \qquad K_d^{E_2} = \begin{cases} -k_{E_2}F_2(C_A) \text{ for } A \\ k_{E_2}F_2(C_A) \text{ for } B \end{cases} \tag{7}$$

Here, k_{E_1} and k_{E_2} are respectively the reaction rates of the enzymatic patches $\boldsymbol{E}_1$ and $\boldsymbol{E}_2$. The reaction rates are given by the products of the reaction rate per molecule of enzyme k_e (in units of s^{-1}) and the areal concentration of enzyme $[E]$ (in units of mol m^{-2}). Thus, the reaction rate can be varied by changing the areal concentration of the enzymes. The width of both the patches along the length of the sheet is w, and thus, the catalytic area of both enzymatic patches are assumed to be same. The functions $F_1(C_B)$ and $F_2(C_A)$ describe the inhibition and promotion reactions that depend on the concentration of chemicals at the patches.

$$F_1(C_B) = \frac{1}{1 + (C_B/K_B)^{n_1}}, \qquad F_2(C_A) = \frac{(C_A/K_A)^{n_2}}{1 + (C_A/K_A)^{n_2}} \tag{8}$$

The above functions mimic the biosynthesis pathway of glutathione. Here, K_B and K_A are, respectively, the inhibition and dissociation constants. The dependence of the functions on the concentration of chemicals A and B is plotted in Figure S1. The plots demonstrate that the rate of production of chemical A at the enzymatic patch E_1 decreases with an increase in the concentration of chemical B, C_B (inhibition of chemical A), whereas the rate of production of chemical B at the enzymatic patch E_2 increases with an increase of the concentration of chemical A, C_A (promotion of chemical B). Note that the rate of consumption and production of chemicals also depend on the cooperativity parameter n_1 and n_2.

We use no-slip boundary conditions for the fluid flow ($\boldsymbol{u} = 0$) and no-flux conditions for chemical C_i at the confining walls of the chamber (at $z = 0$ and $z = H$):

$$\boldsymbol{u}(z = 0) = \boldsymbol{u}(z = H) = 0$$

https://doi.org/10.1021/acs.langmuir.2c02666
Langmuir 2023, 39, 780−789

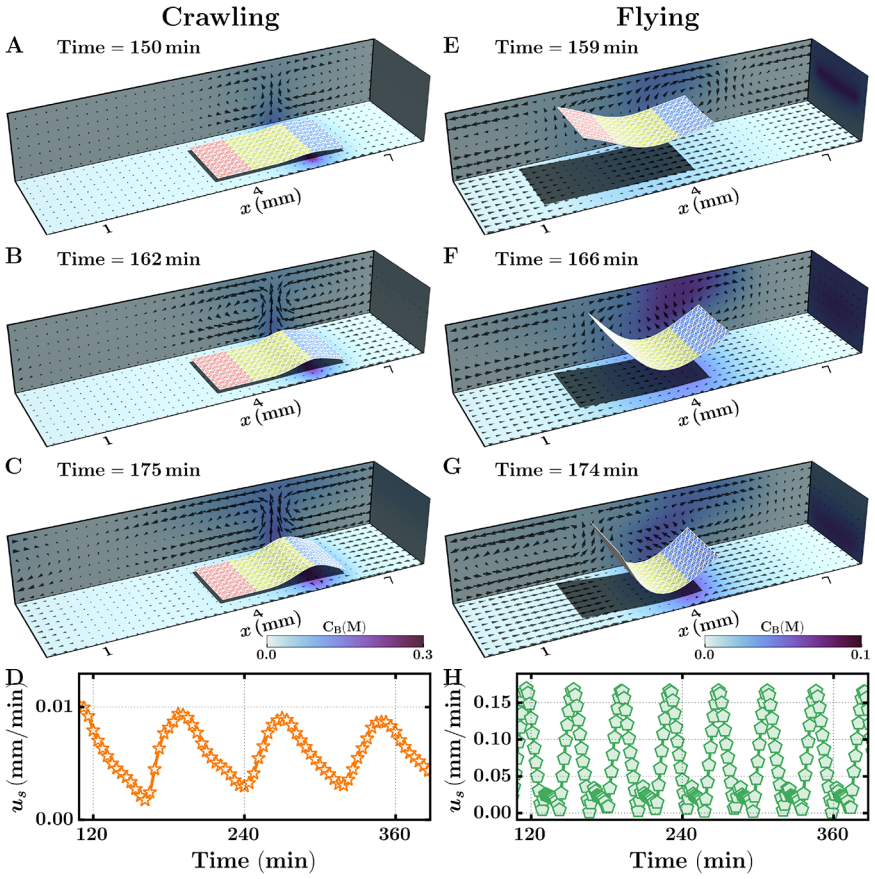

Figure 2. Multimodal locomotion of enzyme-coated elastic sheets. For cases (A–D), the respective solutal expansion coefficients of chemicals A and B are $\beta_A = 0$ and $\beta_B = 0.38 \times 10^{-3}$ M^{-1} (A–C) Crawling motion of the enzyme-coated sheet propelled in the positive x-direction. Inward fluid flow generated at E_2 (blue strip on the sheet) lifts the right end of the sheet and propels it forward (B, C) Black arrows indicate the direction and magnitude of the fluid flow; the arrows on the left vertical wall reveal the flows within a vertical plane passing through the center of the chamber. Arrows on the right sidewall indicate the flow in the orthogonal vertical plane. The color bar indicates the concentration of chemical B in the solution. (D) The propulsion speed of the sheet in the horizontal direction increases periodically as the sheet undergoes the crawling motion. For cases (E–G), the respective solutal expansion coefficients of chemicals A and B are $\beta_A = 0.17 \times 10^{-3}$ M^{-1} and $\beta_B = 0.84 \times 10^{-3}$ M^{-1}. Inward fluid flow generated at both enzymatic patches (red and blue strips) lifts both ends of the sheet and drives the periodic motion of the sheet in the positive x-direction, mimicking a flying motion. (H) The propulsion speed of the sheet in the horizontal direction shows periodic oscillations as the two ends of the sheet. The differences in the periodicity of the oscillation reflect the time delay associated with A reaching the second patch. Stretching and bending moduli of the sheet are $\kappa_s = 60$ pN and $\kappa_b = 6.75$ pN mm^2, respectively. The respective width of the patches, distance between patches, and reaction rate of the enzymatic patch E_1 are 0.77 mm, 2.78 mm, and 74 μmol m^{-2}s^{-1}, respectively.

$$\frac{\partial C_i}{\partial z}(z=0) = \frac{\partial C_i}{\partial z}(z=H) = 0$$

For periodic boundary conditions in the x and y directions, we set

$$\boldsymbol{u}(x=0) = \boldsymbol{u}(x=L_x)$$

$$\boldsymbol{u}(y=0) = \boldsymbol{u}(y=L_y)$$

$$C_i(x=0) = C_i(x=L_x)$$

$$C_i(y=0) = C_i(y=L_y)$$

The governing equations are solved numerically using the lattice Boltzmann method (LBM) with a single relaxation-time D3Q19 scheme[37] to solve the continuity and Navier–Stokes equations (eqs 3 and 4). A finite difference approach with a forward-time central-space (FTCS) scheme is used to solve the equation for advection, diffusion, and reaction of the chemicals (eq 6). The boundary condition for the fluid flow at the confining walls of the chamber satisfies the no-slip boundary condition ($\boldsymbol{u}= \boldsymbol{0}$). For the concentration of chemical C_i, we use a no-flux condition such that no chemical penetrates through the walls, $\frac{\partial C_i}{\partial n} = 0$. Here, $\hat{\boldsymbol{n}}$ is the surface normal pointing into the fluid domain.

The immersed boundary (IB) approach is used to capture the fluid–structure interactions between the elastic sheet and fluid.[35] Each node of the elastic sheet is represented by a sphere with an effective hydrodynamics radius a that accounts for a fluid drag characterized by the mobility $M = (6\pi\mu a)^{-1}$, where $\mu = \nu\rho_0$ is the dynamic viscosity of the fluid. The fluid is an aqueous solution, and we take $\nu = 10^{-6}$ m^2 s^{-1} and $\rho_0 = 10^3$ kg m^{-3}. The forces exerted by the nodes of the elastic sheet on the fluid, calculated using the IB method, provide zero fluid velocities at the discretized nodes of the elastic sheet. Therefore, the IB approach approximates no-slip boundary conditions for the fluid velocities at the nodes. The separation between the nodes of the sheet is sufficiently small that there is no fluid permeation through the nodes constituting the sheet. Since the elastic sheet in our model is composed of one layer of the nodes, the effective thickness, b, of the elastic sheet is equal to the diameter $2a$ of a single node. We keep the thickness of the sheet constant and vary the elastic moduli to alter the mechanical properties of the sheet. Since the sheet is formed from one layer of nodes, both sides of the sheet are assumed to be catalytically active.

https://doi.org/10.1021/acs.langmuir.2c02666
Langmuir 2023, 39, 780–789

The velocity field $\boldsymbol{u}(u_x, u_y, u_z)$ computed using the LBM method at each time step of the simulation is used to advect the chemical concentration (eq 6) and to update the position of nodes of the elastic sheet (eq 5). The updated concentration field is then used to determine the buoyancy forces in eq 2. The time step size, Δt, in the simulation is 2.5×10^{-3} s. The sizes of the computational domain are $82\Delta x \times 22\Delta x \times 17\Delta x$, where the lattice Boltzmann unit Δx is 103 μm. The hydrodynamic radius of the node, a, is taken as $1.3\Delta x$. In the discretization of the elastic sheet, the distance between two nearest neighboring nodes is set to $1.5\Delta x$. The width of the catalytic patches and distance between them are given in Table S3.

For simplicity, we reduce the number of model parameters and choose $D_A = D_B = D$, $K_A = K_B = K$, and $n_1 = n_2 = n$. We took the smallest cooperativity parameter, $n = 3$, that supports the chemical oscillations controlled by the non-linear functions in eq 8. We fix the ratio of the reaction rates k_{E_1}/k_{E_2}= const≈0.0288 and vary reaction rates at the enzymatic patch E_1,k_{E_1}, to obtain different locomotion modes. The parameters relevant to chemical reactions are given in Supplementary Tables S1 and S2.

RESULTS AND DISCUSSION

Multimodal Locomotion of Enzyme-Coated, Elastic Sheets. We focus on the self-propulsion of a rectangular, elastic sheet that is 2.93 mm × 1.4 mm × 0.27 mm in size along the respective x, y, and z directions. The sheet is immersed in an aqueous solution and is initially placed parallel to the bottom wall of the chamber (Figure 1A). The addition of the substrate (reactants), S, activates the reactions in eqs 1 and 2 at the respective surface-anchored, enzymatic patches, E_1 and E_2. We assume that the concentration of S remains constant in the course of the reaction (as would occur if this concentration is sufficiently high). The concentrations of A and B, however, are modulated by the feedback loop in the system, where A promotes the production of B and B in turn suppresses the production of A. We specifically chose the reaction rates in eqs 1 and 2 to be above a critical value so that the A and B concentrations exhibit pronounced oscillations within the chamber.[10]

For the reactions considered below, the density of the products is different than that of the reactants, and thus, the system generates solutal buoyancy-driven fluid flow, which in turn alters the position and shape of the elastic sheet.[3] The signs of the respective solutal buoyancy coefficients for chemicals A and B, β_A and β_B, determine the direction of flow at the enzymatic patches (Figure 1B). For example, $\beta_A > 0$ indicates that the solution containing A is lighter than the pure aqueous solution. The A-rich fluid initially rises upward at the center of the E_1 patch; since the fluid is confined in the chamber, it then flows downward along the sidewalls and inwards (toward E_1) along the bottom surface. In the case that $\beta_B < 0$, the B-containing solution is heavier than the aqueous solution. Hence, the dense B-rich solution produced at E_2 initially flows along the bottom wall, away from the patch, to create outward flow (see Figure 1B). Figure S2 illustrates other examples of the flow patterns for different values of β_A and β_B.

As noted above, the values of β_i are known for a range of catalytic reactions. Here, we choose representative values of β_i to probe the range of potential behavior exhibited by the system. In particular, we consider cases where either the reaction at E_1 or E_2 plays the dominant role to isolate the relative effects of the two patches. We also examine scenarios where β_A and β_B are opposite in sign to determine the overall influence of counteracting flows.

Figure 2 shows the variety of biomimetic motion elicited from the sheet, ranging from "crawling" to "flying". For the crawling motion (Figure 2A−C), $\beta_A = 0$ and $\beta_B = 0.4 \times 10^{-3}$ M^{-1}. With $\beta_A = 0$, the A-containing solution has the same density as the pure aqueous solution and hence does not contribute to buoyancy-driven flow (Figure S3). Namely, the reaction does not spontaneously generate fluid flow above E_1. Conversely, with $\beta_B > 0$, the density of the B-containing fluid is less than that of water and the resultant density gradient produces inward flow centered at E_2. The generated flow in turn drags the sheet upward, above the middle of the E_2 patch (Figure 2B,C and Movie S1). As anticipated from our prior results,[10] the fluid velocity is highest in regions with the greatest concentration of B (see color bar indicating the concentration of B; Figure 2A and Figure S4). Since E_2 lies at the right end of the sheet, the inward fluid flow generates the largest drag forces in the positive x-direction, driving the sheet to move to the right (Figure 2B,C and Movie S1).

As the reaction proceeds, the circulating flow generated at E_2 advects a concentration of A to E_2, where it is consumed to form B, and thus, this concentration decreases with time. With less A in the system, the production of B also decreases, as does the inward fluid flow at E_2. With the decrease in the solutal buoyance forces, the restoring forces due to the elasticity of the sheet and gravity drive the sheet to assume a flat configuration (Movie S1). Concomitantly, as A is advected away from E_1, the latter catalytic patch is "swept clean" and the substrate S in the solution reactivates the reaction at E_1 and the renewed production of A. Consequently, the motion displays cyclic behavior, where the next crawling cycle begins when a sufficient amount of A is advected to E_2 to trigger the reaction in eq 2.

The presence of feedback (between the reactions at E_1 and E_2) is necessary to achieve this cyclic motion and the concomitant periodic oscillations in the concentration of A and B (Figure 2D and Figure S3). The time delay between the oscillation peak for A and B (Figure S3) is due to the spatial separation between the enzymatic patches and can be altered by changing the distance between these domains.

In the ensuing studies, we fix the density of the sheets, the spatial layout of the enzymatic patches, and the feedback loop to be the same as above but alter the values of β_i to $\beta_A = 0.17 \times 10^{-3}$ M^{-1} and $\beta_B = 0.84 \times 10^{-3}$ M^{-1} (Figure 2E−G and Movie S2). Since the sign of the solutal coefficients for both chemicals A and B are positive, both chemical solutions are less dense than the aqueous solution. Thus, the production of chemicals A and B produces inward fluid flow about the respective patches, E_1 and E_2. The generated flows lift both patches upward, with the sheet appearing to "fly" (Figure 2E−G and Movie S2). (The "flying" motion resembles the flapping of wings, but the sheet does remain in the fluid.) The plots for the solutal buoyancy force $\boldsymbol{F}^b = \boldsymbol{g}\rho_0 \sum \beta_i C_i$ due to both chemicals A and B (see Figure S6) show that at any point in time, the magnitude of the solutal buoyancy force is higher on E_1 than E_2. The resulting asymmetry in the fluid flow drives the sheet in the positive x-direction (Movie S2). Due to the feedback loop and chosen values of the parameters (Table S1), the sheet displays periodic motion reflecting the chemical oscillations in the solution. Since the patches are spatially separated, there is a time delay between the two reactions and a resultant difference in the peaks for the $\boldsymbol{F}^b$ (Figure S5B).

In the above cases, the chemicals produced at the patches cause the local fluid to be lighter than the aqueous solution. If

https://doi.org/10.1021/acs.langmuir.2c02666
Langmuir 2023, 39, 780−789

the dissolved chemicals lead to a solution that is denser than water, then we observe different modes of locomotion. For example, the sheet undergoes a "swimming motion" when $\beta_A = 0$ and $\beta_B = -1.7 \times 10^{-3}\mathrm{M}^{-1}$ (Figure S7 and Movie S3). With $\beta_A = 0$, the A produced at E_1 has the same density as the host fluid and hence does not contribute to buoyancy-driven flow. Conversely, the production of the denser B at E_2 generates outward fluid flow, with the denser fluid initially moving away from the center of E_2. The latter flow profile constrains this patch to remain localized at the bottom of the chamber (Figure S8). Due to the continuity of the confined fluid, a portion of the convective roll generated at E_2 gives rise to an upward drag on E_1 (as the fluid circulates back downward toward E_2) that lifts this portion of the sheet (Figures S7 and S8). Since these drag forces act on the left end of the sheet (Figure S7), the entire sheet moves in the negative x-direction. This propulsion continues until the production of B at E_2 is sufficiently low that the magnitude of outward fluid flow becomes relatively small, as does the resultant upward flow at E_1. Consequently, the entire sheet assumes a flat configuration (Movie S3). The substrate S, however, triggers new production of A at E_1, and the next swimming cycle begins when a sufficient amount of A reaches E_2. These periodic oscillations of chemicals A and B in the chamber enable the sheets to display the continuous swimming motion.

The above examples illustrate the intimate coupling among chemistry, flow, and the structure of the sheet. Namely, the inherent catalytic reactions spontaneously generate fluid motion, which in turn applies a force on the sheet that both alters its form and transports the sheet in a particular direction. The system displays chemo-mechanical transduction as the chemical reaction affects the oscillations of the sheet and the oscillations of the sheet affect the chemistry. Once the reactants are added to the solution, the entire process occurs seamlessly and autonomously.

Chemo-Mechanical Feedback. As described above, the chemical reactions at the enzymatic patches induce chemical oscillations, which in turn give rise to the mechanical oscillations of the sheet. Moreover, the mechanical oscillations can affect the chemical oscillations in the chamber. To investigate this feedback between chemical and mechanical behavior, we vary the bending rigidity, k_b, of the sheet while keeping the values that characterize the enzymatic reaction and patches fixed. Here, we set $\beta_A = 0$ and $\beta_B = -1.7 \times 10^{-3}\mathrm{M}^{-1}$, for which the system exhibits oscillatory swimming motion.

If the system exhibits chemo-mechanical feedback, then the amplitude of the chemical oscillations will depend on the system's mechanical behavior, characterized by k_b. Recall that chemical oscillations occur within a specific range of system parameters,[10] including values of k_b. If the characteristic values of the chemical reaction lie outside this range, then the behavior of the system can be localized in the non-oscillatory regime. These two features are reflected in Figure 3A, which shows that: (1) that the amplitude of oscillations of chemical A are dependent on k_b, and (2) the amplitude of the chemical oscillations initially increases with increases in k_b and then appears to reach a plateau value. The first point highlights the chemo-mechanical coupling in the oscillatory regime, while the second point emphasizes that the coupling occurs only for a finite range of k_b. Beyond a critical value of k_b, the concentration of A remains constant.

The plot in Figure 3B shows that the amplitude of the mechanical oscillations decreases with an increase in the

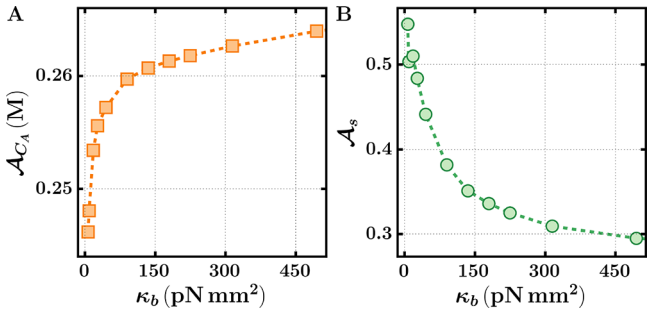

Figure 3. Chemo-mechanical feedback in the locomotion of the enzyme-coated elastic sheet. (A) The amplitude of oscillations of chemical A is plotted as a function of the bending modulus of the sheet. (B) The amplitude of sheet oscillation decreases with an increase in the bending modulus of the sheet. The stretching modulus of the sheet and physical dimensions of the patches are the same as in Figure 2. The reaction rates of the enzymatic patches are the same as in Figure 2. The solutal expansion coefficients of chemicals A and B are $\beta_A = 0$ and $\beta_B = -1.7 \times 10^{-3}$ M^{-1}.

bending rigidity of the sheet. At higher values of k_b, the restoring forces inhibit deformation of a stiffer sheet. Taken together, Figure 3A,B provides further insight into the cross-talk between mechanics and chemistry. In particular, a comparison of the figures shows that the decrease in the amplitude of the mechanical oscillations (Figure 3B) coincides with an increase in the amplitude of the chemical oscillations (Figure 3A). With less energy dissipated in mechanical behavior, a greater portion of the energy released from the reaction is dissipated through oscillatory motion of the fluid and chemical transport. In other words, the system also exhibits mechano-chemical feedback, where the mechanical oscillations affect the magnitude of the chemical oscillations.

Non-Oscillatory, Self-Sustained Motion. In the following simulations, the values of β_A and β_B were specifically chosen to localize behavior of the system in the non-oscillatory regime. (Figure S9 clearly shows the lack of chemical oscillations in this system.) Nonetheless, the systems display a coupling between chemistry and spontaneous, self-sustained locomotion, as shown in the examples below. For the solutal expansion coefficient $\beta_A = -0.33 \times 10^{-3}$ M^{-1} and $\beta_B = -0.67 \times 10^{-3}$ M^{-1}, the sheet now displays a continuous sliding motion (Figure S9 and Movie S4). The production of A at E_1 and the conversion of A to B at E_2 generate a chemical gradient across the length of the sheet, as evidenced by the non-uniform distribution of B in Figures S9A–C. As the sheet traverses the chamber (Figure S10), the highest concentration of B remains localized above the E_2 production site.

The generated chemical gradient produces solutal buoyancy forces that drag the sheet in the positive x-direction (Movie S4). Since the sign of both solutal expansion coefficients is negative, fluid flow is outward, pushing the sheet to assume a flat, 2D configuration at the bottom of the chamber. Nevertheless, the chemical gradients arising from the coupled reactions generate a force that drives a steady fluid flow that maintains the directed sliding of the layer in the channel.

It is important to note that the fluid flow generated in the non-oscillatory regime is still effective at morphing a 2D sheet into a 3D structure. For solutal expansion coefficients $\beta_A = -0.16 \times 10^{-3}$ M^{-1} and $\beta_B = 0.8 \times 10^{-3}$ M^{-1}, the enzymatic patch E_1 generates inward fluid flow and the E_2 patch drives outward fluid flow at their respective locations. The magnitude of the

https://doi.org/10.1021/acs.langmuir.2c02666
Langmuir 2023, 39, 780−789

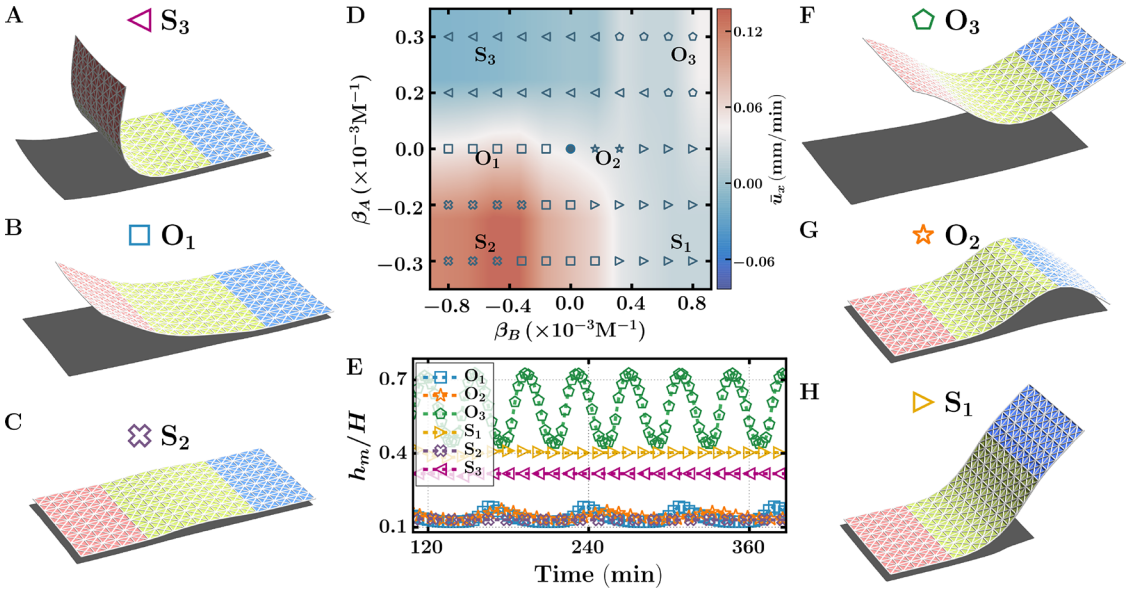

Figure 4. State diagram of the various locomotion modes of the enzymatic-coated elastic sheet. (A−C, F−H) Representative configurations of different locomotion modes of the sheet. (D) State diagram of the enzyme-coated elastic sheets as a function of solutal coefficients of chemicals *A* and *B*. The respective crawling, flying, and swimming motions of the sheet are marked by a star, pentagon, and square, respectively. In the latter modes of locomotion, both chemicals in the solution and the sheet oscillate periodically. Modes of non-oscillatory motion in the positive and negative *x*-direction are respectively marked by the right- and left-pointing triangles. The non-oscillatory motion of an essentially flat sheet is marked by an x. (E) The height of the center of mass of the sheet as a function of time shows the oscillatory and non-oscillatory behavior of different locomotion modes. The stretching and bending moduli of the sheet, physical dimensions of the patches, and the reaction rates of the enzymatic patches are the same as in Figure 2.

upward drag (part of the dynamic convective roll) at patch E_2 is sufficiently large that the fluid flow lifts the right end of the sheet to the top of the chamber (Figure S11A−C). At the same time, the downward fluid flow at patch E_1 keeps the left end of the sheet at the bottom surface of the chamber (Figure S11A). The sheet remains in this 3D configuration, and the resulting fluid drag on the sheet drives the sheet in the positive *x*-direction (Movie S5).

The sheet's direction of the propulsion can be changed by changing the sign of the solutal expansion coefficient. For $\beta_A = 0.16 \times 10^{-3}$ M^{-1} and $\beta_B = -0.8 \times 10^{-3}$ M^{-1}, the inward fluid flow at the patch E_1 lifts the left end of the sheet to the top of the chamber and the outward flow at patch E_2 keeps the right end of the sheet at the bottom of the chamber (Figure S12A−C). The resulting fluid drag on the sheet acts in the negative *x*-direction, driving the sheet in that path (Figure S12 and Movie S6).

State Diagram. By performing systematic variations in the solutal expansion coefficients, we can generate the state diagram in Figure 4, which delineates the various modes of locomotion as a function of β_A and β_B. The plot reveals the existence of three oscillatory locomotion modes (marked by O_1, O_2, and O_3) and three static locomotion modes (marked by S_1, S_2, and S_3). In the oscillatory modes, the moving sheets exhibit periodic variations in shape (Figure 4E), while in the static locomotion modes, the moving sheet assumes a fixed configuration (Figure 4E).

The propulsion speed is different for the different locomotion modes and is indicated by the color bar in Figure 4D. The maximum propulsion speed is observed for the case of the sliding motion (S_2 state) as the fluid drag acts in the same direction for all nodes of the sheet. The propulsion speed is minimum for the case of S_1 and S_3 states as the fluid drag on the top and bottom of the sheet act in the opposite directions.

The above state diagram was obtained for a constant reaction rate at the enzymatic patch, k_{E_1}. As discussed below, the state diagram can be tuned by altering the reaction rate at the patch.

Influence of the Reaction Rate, Width of the Patch, and Distance between Patches. Focusing on the oscillatory swimming movement (O_1 state), we investigate the effect of varying the reaction rate, patch width, and distance between patches on the oscillations and propulsion of the sheet in the chamber. We choose the respective solutal expansion coefficients of chemicals *A* and *B* as $\beta_A = 0$ and $\beta_B = -1.7 \times 10^{-3}$ M^{-1}. Figure 5B shows that the increase in the reaction rate at patch E_1 increases the amplitude of the oscillations for *A* and consequently increases the amplitude of oscillations for *B* (Figure S13). An increase in the oscillation amplitude for *B* increases the buoyancy forces that act on the fluid and concomitantly increases the velocities of the fluid flow (producing the outward flow at patch E_2 and upward flow near the patch E_1). The latter behavior gives rise to increases in the height of the amplitude attained by the sheet (Figure 5C).

The amplitudes of these chemical and sheet oscillations are plotted respectively in Figure 5D and Figure 5E as a function of the chemical reaction rate at the enzymatic patch E_1 for two different widths of the patches. There exists a critical reaction rate, $k_{E_{1c}}$, below which there are no oscillations of chemicals (Figure 5D). For reaction rate $k_{E_1} > k_{E_{1c}}$, the amplitude of the chemical and sheet's oscillations increases with the increasing reaction rate.

Since chemical gradients across the length of the sheet are lower for the wider patches (since all other parameters are held fixed), the amplitude of the chemical oscillations is lower for the larger path width. As a result, the upward fluid flow and the amplitude of the sheet oscillations are lower for the larger

https://doi.org/10.1021/acs.langmuir.2c02666
Langmuir 2023, 39, 780−789

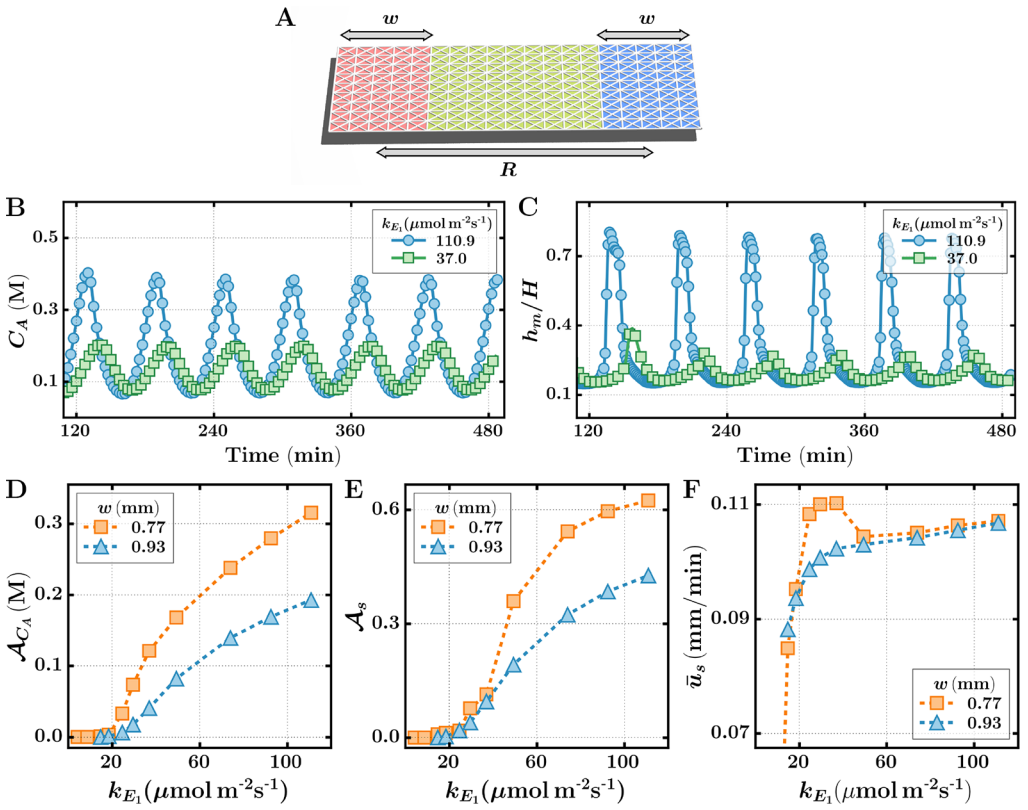

Figure 5. Effect of varying reaction rate, width of the patch, and distance between patches on swimming locomotion. (A) Schematic diagram of the enzyme-coated sheet that illustrates patch width and distance between patches. (B) Oscillations of chemical concentration A for different reaction rates at enzymatic patch E_1. (C) Height of the center of mass of the sheet as a function of time. The width of the patches and distance between patches in (A) and (B) are, respectively, 0.77 and 2.78 mm. (D, E) Amplitude of the chemical oscillations (D) and sheet oscillations (E) as a function of the reaction rate at the patch E_1 for different widths of the patches. (F) The propulsion speed increases with the increase in reaction rate, k_{E_1}. The distance between patches in (D–F) is R = 2.78 mm. The stretching and bending moduli of the sheet are the same as in Figure 2. The solutal expansion coefficients of chemicals A and B are $\beta_A = 0$ and $\beta_B = -1.7 \times 10^{-3}\text{M}^{-1}$.

width (Figure 5E). Relative to the wider patch, the narrow patch generates an increase in the amplitude of the sheet oscillations and increases the sheet's propulsion speed in the horizontal direction (Figure 5F).

In addition to reaction rate and width of the patches, the chemical oscillations and locomotion of the sheet can also be altered by changing the distance between the two patches, R. The amplitudes of chemical and sheet oscillations are plotted in Figure S14A,B as a function of R for two widths of the patches at a constant reaction rate at the patch k_{E_1} = 74 μmol m^{-2} s^{-1}. For both patch widths, oscillations are only observed for a separation distance larger than a critical distance, $R > R_c$. This critical distance between the patches is approximately R_c = 1.6 mm for the reaction rate k_{E_1} = 74 μmol m^{-2} s^{-1}. The distance between patches also affects the sheet's propulsion speed (Figure S14C), which increases linearly with an increase in the distance between patches (up to some critical separation).

CONCLUSIONS

We simulated various modes of self-propulsion exhibited by chemically active, flexible sheets immersed in solution. The chemical activity involved a two-step promotor–inhibitor reaction catalyzed by two surface-anchored catalytic patches. Even though this two-step loop appears to be relatively simple, it nonetheless is a key modular unit in extensive, interlinked biochemical reactions.

The chemical reactions promoted by the separated catalytic patches generate solutal buoyancy driven flows. In this way, the system mimics biological chemo-mechanical transduction as chemical input is converted into mechanical output. The resulting convective vortices, which exert drag forces on the ends of the sheet, enabled the sheet to move along the fluid-filled channel.

In the observed oscillatory regimes, the flow arising from the oscillating chemical reactions produced oscillatory mechanical deformation in the sheet, as evidenced by the corresponding regular periodic behavior in the sheet height as a function of time. Moreover, as shown in Figure 3, the mechanical oscillations affected the magnitude of the chemical oscillations, revealing the complexity of the cross-talk between chemistry and mechanics in the system.

Specific modes of oscillatory propulsion were activated through a judicious choice of reagents, which have appropriate solutal expansion coefficients and generate apt directions of the fluid flows (inward or outward) at each sheet end. In the non-oscillatory regime, the fluid still morphed the sheet, but the deformed sheet was simply translated along the length of the channel.

In both the oscillatory and non-oscillatory regimes, the effect of varying the system's parameters is described by the dimensionless Grashof number, Gr = $g\beta C_0 H^3/\nu^2$, which

https://doi.org/10.1021/acs.langmuir.2c02666
Langmuir 2023, 39, 780–789

quantifies the relative contributions of solutal buoyancy and the viscous forces acting in the system. Here, β is the coefficient of solutal expansion and C_0 is the characteristic chemical variation across the domain. In particular, Gr implies that the flow velocities can be increased by using chemicals with higher expansion coefficients as well as increasing the characteristic concentration of chemicals or increasing the height of the chamber. To facilitate future experimental studies, we estimate that Gr ≈ 270 (corresponding to Figure 2A−C) in our simulations, indicating the dominating influence of solutal buoyancy in the system. Notably, there exist both synthetic[38−41] and biological[42−44] thin films that exhibit a comparable flexural rigidity to our model sheet. With the anchoring of catalysts on the surface, these thin films can be utilized for future experimental studies.[41,45]

The different values of the buoyancy coefficients β_i used herein correspond to different chemicals in the solution. Catalytic reactions are typically selective: only certain reactants can instigate specific reactions. For practical applications, the chemical composition of the catalytic patches would ideally remain fixed and only the reactants (and the resultant products) would be altered as a given sheet is placed in a new solution. In this scenario, the sheet could serve as an adaptive sensor, changing its mode of locomotion to indicate changes in the chemical environment.

With respect to other applications, the shape of the sheets can be fashioned by using appropriate chemistry. In particular, a specific chemical environment autonomously enables fluid flows that sculpt a sheet into a particular shape, which in turn enables a certain functionality. In this sense, form and function are intimately related in these systems. For example, the chemical solution in Figure 2E−G formed "wings" and thus created a useful form for "flying".

While models for CRNs can describe more complex chains of reactions, few models typically encompass a description of the spatial layout of the network. Figure S14A,C clearly shows that the separation between the two patches affects the amplitude of the chemical oscillations and velocity of locomotion. It is also evident that the placement of the patches contributed to the observed shape changes, since this placement affects the location of the convective flows, which effectively control the sheet's morphological evolution. The symmetric, terminal location of the patches was needed to create the wings seen in Figure 2. These findings underscore the importance of the spatial relationships of the reactive "nodes" in CRNs in dictating global dynamics.

In addition to the relative spatial arrangement of the reaction sites, the influence of solutal buoyancy is frequently neglected in descriptions of flow within the human body. Fluids in the body are confined between structural walls (e.g., between cell walls) and sequestered in chambers that are on the micrometer scale. The system of the confined fluid and confining walls is referred to as the "interstitum".[19] These fluid-filled interstitial spaces form a continuous network that spans the entire body; the fluid volume in the interstitium is approximately 20% of body weight.[19] While it is recognized that fluids pumped through the body by the circulatory system can produce shear stresses on confining walls, it is reasonable to assume that chemical reactions occurring within the confined domains can generate solutal buoyance forces that deform the biological confining walls. The deformed walls can in turn affect biological function; this connection between the solutal buoyancy mechanism, the morphing of the confining walls, and the functioning of the surrounding tissue remains to be discovered.

■ ASSOCIATED CONTENT

Supporting Information

The Supporting Information is available free of charge at https://pubs.acs.org/doi/10.1021/acs.langmuir.2c02666.

(Movie S1) "Crawling" motion of an enzyme-coated elastic sheet (MP4)

(Movie S2) "Flying" motion of an enzyme-coated elastic sheet (MP4)

(Movie S3) "Swimming" motion of an enzyme-coated elastic sheet (MP4)

(Movie S4) "Sliding" motion of an enzyme-coated elastic sheet (MP4)

(Movie S5) Non-oscillatory motion of an enzyme-coated elastic sheet in the positive x-direction (MP4)

(Movie S6) Non-oscillatory motion of an enzyme-coated elastic sheet in the negative x-direction (MP4)

Model of elastic sheet, simulation parameters, and supplementary figures (PDF)

■ AUTHOR INFORMATION

Corresponding Author

Anna C. Balazs − *Department of Chemical Engineering, University of Pittsburgh, Pittsburgh, Pennsylvania 15260, United States;* orcid.org/0000-0002-5555-2692; Email: balazs@pitt.edu

Authors

Raj Kumar Manna − *Department of Chemical Engineering, University of Pittsburgh, Pittsburgh, Pennsylvania 15260, United States;* orcid.org/0000-0003-2272-9487

Oleg E. Shklyaev − *Department of Chemical Engineering, University of Pittsburgh, Pittsburgh, Pennsylvania 15260, United States;* orcid.org/0000-0002-9242-9255

Complete contact information is available at: https://pubs.acs.org/10.1021/acs.langmuir.2c02666

Author Contributions

All authors contributed to all aspects of the article.

Notes

The authors declare no competing financial interest.

■ ACKNOWLEDGMENTS

We gratefully acknowledge funding from Department of Energy under grant DE-FG02-90ER45438, the Department of Defense, Army Research Office under grant W911NF-17-1-0351 and the computational facilities at the Center for Research Computing at the University of Pittsburgh.

■ REFERENCES

(1) Zhang, Y.; Hess, H. Chemically-Powered Swimming and Diffusion in the Microscopic World. *Nat. Rev. Chem.* **2021**, *5*, 500−510.

(2) Sánchez, S.; Soler, L.; Katuri, J. Chemically Powered Micro- and Nanomotors. *Angew. Chem., Int. Ed.* **2015**, *54*, 1414−1444.

(3) Manna, R. K.; Laskar, A.; Shklyaev, O. E.; Balazs, A. C. Harnessing the Power of Chemically Active Sheets in Solution. *Nat. Rev. Phys.* **2022**, 125−137.

(4) Liebchen, B.; Löwen, H. Synthetic Chemotaxis and Collective Behavior in Active Matter. *Acc. Chem. Res.* **2018**, *51*, 2982−2990.

(5) Wang, W.; Duan, W.; Ahmed, S.; Mallouk, T. E.; Sen, A. Small Power: Autonomous Nano- and Micromotors Propelled by Self-Generated Gradients. *Nano Today* **2013**, *8*, 531−554.
(6) Ebbens, S. J. Active Colloids: Progress and Challenges towards Realising Autonomous Applications. *Curr. Opin. Colloid Interface Sci.* **2016**, *21*, 14−23.
(7) Gregory, D. A.; Ebbens, S. J. Symmetrical Catalytically Active Colloids Collectively Induce Convective Flow. *Langmuir* **2018**, *34*, 4307−4313.
(8) Jez, J. M.; Cahoon, R. E. Kinetic Mechanism of Glutathione Synthetase from Arabidopsis Thaliana*. *J. Biol. Chem.* **2004**, *279*, 42726−42731.
(9) Jez, J. M.; Cahoon, R. E.; Chen, S. Arabidopsis Thaliana Glutamate-Cysteine Ligase: Functional Properties, Kinetic Mechanism, and Regulation of Activity. *J. Biol. Chem.* **2004**, *279*, 33463−33470.
(10) Shklyaev, O. E.; Yashin, V. V.; Stupp, S. I.; Balazs, A. C. Enhancement of Chemical Oscillations by Self-Generated Convective Flows. *Commun. Phys.* **2020**, *3*, 1−9.
(11) van Roekel, H. W. H.; Rosier, B. J. H. M.; Meijer, L. H. H.; Hilbers, P. A. J.; Markvoort, A. J.; Huck, W. T. S.; de Greef, T. F. A. Programmable Chemical Reaction Networks: Emulating Regulatory Functions in Living Cells Using a Bottom-up Approach. *Chem. Soc. Rev.* **2015**, *44*, 7465−7483.
(12) Semenov, S. N.; Kraft, L. J.; Ainla, A.; Zhao, M.; Baghbanzadeh, M.; Campbell, V. E.; Kang, K.; Fox, J. M.; Whitesides, G. M. Autocatalytic, Bistable, Oscillatory Networks of Biologically Relevant Organic Reactions. *Nature* **2016**, *537*, 656−660.
(13) Merindol, R.; Walther, A. Materials Learning from Life: Concepts for Active, Adaptive and Autonomous Molecular Systems. *Chem. Soc. Rev.* **2017**, *46*, 5588−5619.
(14) Semenov, S. N.; Wong, A. S. Y.; van der Made, R. M.; Postma, S. G. J.; Groen, J.; van Roekel, H. W. H.; de Greef, T. F. A.; Huck, W. T. S. Rational Design of Functional and Tunable Oscillating Enzymatic Networks. *Nat. Chem.* **2015**, *7*, 160−165.
(15) Robinson, W. E.; Daines, E.; van Duppen, P.; de Jong, T.; Huck, W. T. S. Environmental Conditions Drive Self-Organization of Reaction Pathways in a Prebiotic Reaction Network. *Nat. Chem.* **2022**, *14*, 623−631.
(16) Hess, B.; Mikhailov, A. Self-Organization in Living Cells. *Ber. Bunsen-Ges. Phys. Chem.* **1994**, *98*, 1198−1201.
(17) Kaneko, K.*Life: An Introduction to Complex Systems Biology*; Springer: Berlin, New York, 2006.
(18) Bhalla, U. S.; Iyengar, R. Emergent Properties of Networks of Biological Signaling Pathways. *Science* **1999**, *283*, 381−387.
(19) Wiig, H.; Swartz, M. A. Interstitial Fluid and Lymph Formation and Transport: Physiological Regulation and Roles in Inflammation and Cancer. *Physiol. Rev.* **2012**, *92*, 1005−1060.
(20) Manna, R. K.; Gentile, K.; Shklyaev, O. E.; Sen, A.; Balazs, A. C. Self-Generated Convective Flows Enhance the Rates of Chemical Reactions. *Langmuir* **2022**, *38*, 1432−1439.
(21) Unsleber, J. P.; Reiher, M. The Exploration of Chemical Reaction Networks. *Annu. Rev. Phys. Chem.* **2020**, *71*, 121−142.
(22) Karsenti, E. Self-Organization in Cell Biology: A Brief History. *Nat. Rev. Mol. Cell Biol.* **2008**, *9*, 255−262.
(23) Epstein, I. R.; Pojman, J. A.*An Introduction to Nonlinear Chemical Dynamics: Oscillations, Waves, Patterns, and Chaos*; Oxford university press, 1998, DOI: 10.1093/oso/9780195096705.001.0001.
(24) Brandman, O.; Meyer, T. Feedback Loops Shape Cellular Signals in Space and Time. *Science* **2008**, *322*, 390−395.
(25) Soh, S.; Byrska, M.; Kandere-Grzybowska, K.; Grzybowski, B. A. Reaction-Diffusion Systems in Intracellular Molecular Transport and Control. *Angew. Chem., Int. Ed.* **2010**, *49*, 4170−4198.
(26) Shklyaev, O. E.; Balazs, A. C. Lifelike Behavior of Chemically Oscillating Mobile Capsules. *Matter* **2022**, *5*, 3464−3484.
(27) Sengupta, S.; Patra, D.; Ortiz-Rivera, I.; Agrawal, A.; Shklyaev, S.; Dey, K. K.; Córdova-Figueroa, U.; Mallouk, T. E.; Sen, A. Self-Powered Enzyme Micropumps. *Nat. Chem.* **2014**, *6*, 415−422.
(28) Valdez, L.; Shum, H.; Ortiz-Rivera, I.; Balazs, A. C.; Sen, A. Solutal and Thermal Buoyancy Effects in Self-Powered Phosphatase Micropumps. *Soft Matter* **2017**, *13*, 2800−2807.
(29) Das, S.; Shklyaev, O. E.; Altemose, A.; Shum, H.; Ortiz-Rivera, I.; Valdez, L.; Mallouk, T. E.; Balazs, A. C.; Sen, A. Harnessing Catalytic Pumps for Directional Delivery of Microparticles in Microchambers. *Nat. Commun.* **2017**, *8*, 14384.
(30) Maiti, S.; Shklyaev, O. E.; Balazs, A. C.; Sen, A. Self-Organization of Fluids in a Multi-Enzymatic Pump System. *Langmuir* **2019**, *35*, 3724−3732.
(31) Hu, W.; Lum, G. Z.; Mastrangeli, M.; Sitti, M. Small-Scale Soft-Bodied Robot with Multimodal Locomotion. *Nature* **2018**, *554*, 81−85.
(32) Ceylan, H.; Dogan, N. O.; Yasa, I. C.; Musaoglu, M. N.; Kulali, Z. U.; Sitti, M. 3D Printed Personalized Magnetic Micromachines from Patient Blood−Derived Biomaterials. *Sci. Adv.* **2021**, *7*, No. eabh0273.
(33) Aghakhani, A.; Yasa, O.; Wrede, P.; Sitti, M. Acoustically Powered Surface-Slipping Mobile Microrobots. *Proc. Natl. Acad. Sci.* **2020**, *117*, 3469−3477.
(34) Zhao, T.; Zhang, Y.; Fan, Y.; Wang, J.; Jiang, H.; Lv, J.-A. Light-Modulated Liquid Crystal Elastomer Actuator with Multimodal Shape Morphing and Multifunction. *J. Mater. Chem. C* **2022**, *10*, 3796−3803.
(35) Lim, S.; Ferent, A.; Wang, X. S.; Peskin, C. S. Dynamics of a Closed Rod with Twist and Bend in Fluid. *SIAM J. Sci. Comput.* **2008**, *31*, 273−302.
(36) Chandrasekhar, S.*Hydrodynamic and Hydromagnetic Stability*; Dover: New York, 1981.
(37) Guo, Z.; Zheng, C.; Shi, B. Discrete Lattice Effects on the Forcing Term in the Lattice Boltzmann Method. *Phys. Rev. E: Stat., Nonlinear, Soft Matter Phys.* **2002**, *65*, No. 046308.
(38) Lin, Y.; Skaff, H.; Böker, A.; Dinsmore, A. D.; Emrick, T.; Russell, T. P. Ultrathin Cross-Linked Nanoparticle Membranes. *J. Am. Chem. Soc.* **2003**, *125*, 12690−12691.
(39) Lee, D. Y.; Pham, J. T.; Lawrence, J.; Lee, C. H.; Parkos, C.; Emrick, T.; Crosby, A. J. Macroscopic Nanoparticle Ribbons and Fabrics. *Adv. Mater.* **2013**, *25*, 1248−1253.
(40) Kim, J.; Hanna, J. A.; Byun, M.; Santangelo, C. D.; Hayward, R. C. Designing Responsive Buckled Surfaces by Halftone Gel Lithography. *Science* **2012**, *335*, 1201−1205.
(41) Na, J.-H.; Evans, A. A.; Bae, J.; Chiappelli, M. C.; Santangelo, C. D.; Lang, R. J.; Hull, T. C.; Hayward, R. C. Programming Reversibly Self-Folding Origami with Micropatterned Photo-Cross-linkable Polymer Trilayers. *Adv. Mater.* **2015**, *27*, 79−85.
(42) Vargo, K. B.; Parthasarathy, R.; Hammer, D. A. Self-Assembly of Tunable Protein Suprastructures from Recombinant Oleosin. *Proc. Natl. Acad. Sci. U. S. A.* **2012**, *109*, 11657−11662.
(43) Mohandas, N.; Evans, E. Mechanical Properties of the Red Cell Membrane in Relation to Molecular Structure and Genetic Defects. *Annu. Rev. Biophys. Biomol. Struct.* **1994**, *23*, 787−818.
(44) Zhelev, D. V.; Needham, D.; Hochmuth, R. M. A Novel Micropipet Method for Measuring the Bending Modulus of Vesicle Membranes. *Biophys. J.* **1994**, *67*, 720−727.
(45) Huang, Y.; Ren, J.; Qu, X. Nanozymes: Classification, Catalytic Mechanisms, Activity Regulation, and Applications. *Chem. Rev.* **2019**, *119*, 4357−4412.

https://doi.org/10.1021/acs.langmuir.2c02666
Langmuir 2023, 39, 780−789